PHYSICAL REVIEW C VOLUME 14, NUMBER 3 SEPTEMBER 1976

Electron scattering from vibrational nuclei

J. W. Lightbody, Jr., S. Penner, and S. P. Fivozinsky
National Bureau of Standards, Washington, D. C. 20234

P. L. Hallowell*† and Hall Crannell*
The Catholic University of America, Washington, D.C. 20064

(Received 18 February 1976)

We present electron scattering form factors for the ground states and several low energy quadrupole excitations of the nuclei ^{52}Cr, ^{110}Pd, ^{114}Cd, and ^{116}Sn. For ^{116}Sn we also present the form factor for the lowest octupole excitation. From these data we derive ground state charge distribution parameters as well as $B(EL)$ values. We attempt to interpret the observed 2^+ states as the one- and two-phonon states of an anharmonic vibrational model. Predictions are made for the electromagnetic decay branching ratios and excited state electric quadrupole moments.

[NUCLEAR REACTIONS $e+{}^{52}$Cr, ^{110}Pd, ^{114}Cd, ^{116}Sn; $\theta=127.5°$, $E=40, 50, 60, 75, 92, 110$ MeV; ground state charge distribution parameters; anharmonic vibrator model fits to quadrupole excitation data.]

I. INTRODUCTION

The vibrational model of the nucleus has found a great deal of qualitative success in describing the low-lying level structure of many nuclei. Figure 1 shows the predicted level scheme and attendant transitions for an even-even, harmonic vibrational nucleus. The basic degree of freedom is the quadrupole shape transition, or single phonon excitation. Dynamically such nuclei exhibit strong $E2$ transitions between states differing by one phonon number ($\Delta n = 1$), while crossover transitions ($\Delta n \geq 2$) are strongly inhibited.

In applying the spherical harmonic vibrator model to predict nuclear observables, one finds that there are several experimental results which disagree with harmonic model predictions. First, the energy level scheme for real nuclei is not as predicted. The physical states which we attempt to identify as two-phonon states are not a degenerate triplet, at twice the excitation energy of the one-phonon state. In fact, the vibrator energy spectrum is in poor agreement with observation at energies above the two-phonon states. A second model inadequacy is the failure to predict the observed nonzero static quadrupole moment for the first excited 2^+ state. This result has been revealed in reorientation effect measurements[1] in which near rotational model values for the first excited state static quadrupole moment of many vibrational nuclei have been reported. [The reorientation effect is a second order Coulomb excitation process in which the strong electric field present during Coulomb excitation of the 2_1^+ state causes the 2_1^+ state magnetic quantum number to change ($m_j \to m_j'$). This is shown symbolically in Fig. 1 as $Q_{22'}$.] The final model shortcoming we wish to discuss concerns electromagnetic decays of the first two excited 2^+ states (2_1^+ and 2_2^+). The measured ratio of $E2$ strengths ($2_2^+ \to 0^+/2_2^+ \to 2_1^+$) and ($2_2^+ \to 2_1^+/2_1^+ \to 0^+$) are not as predicted. The former is in fact considerably larger than harmonic model estimates (of order 10X) while the latter is correct in order of magnitude, but definitely not equal to the simple geometrical factor of 2 arising from angular momentum considerations alone. In an attempt to reconcile and understand these various phenomena, anharmonicities were introduced into the vibrator model.

The present electron scattering experiment was undertaken to investigate the applicability of a simple anharmonic vibrator model in describing the low-lying level structure of several medium atomic weight nuclei: ^{52}Cr, ^{110}Pd, ^{114}Cd, and ^{116}Sn. The basic idea behind the experiment was to perform measurements of the 2_1^+ and 2_2^+ state electron scattering cross sections, and from these measurements deduce the extent to which pure harmonic vibrator one- and two-phonon state wave functions are mixed in the physical 2_1^+ and 2_2^+ states. Theoretical basis for the experiment was presented in an earlier publication,[2] and preliminary Born approximation analysis of our data was presented at the 1972 Nuclear Structure Conference in Sendai, Japan.[3] We herein present final results of our analysis of these data. From our results one can obtain vibrator model wave functions [derived by fitting the (e,e') data] and use them to predict γ ray decay branching ratios of the 2_2^+ states, and the static quadrupole moments for

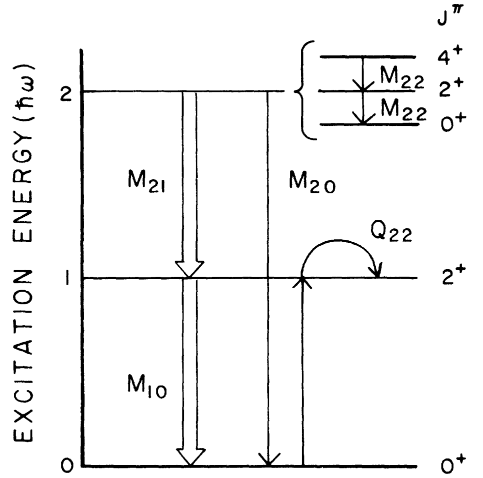

FIG. 1. Level scheme for vibrational nuclei. The full arrows indicate a strong $E2$ transition while the single line arrows indicate a weak transition. The reorientation effect is a two-step process indicated by Q_{22}.

the 2_1^+ and 2_2^+ states. Furthermore, there has been theoretical work based on the dynamic collective model[4] and on the particle-phonon coupling model[5] which predicts the magnitude and phase of the phonon mixing in these 2^+ states. The success of these calculations reconciles the *ad hoc* nature of our somewhat simplistic phonon mixing model.

II. ANHARMONIC MODEL

The electromagnetic transition operator M_{LM} can be expressed in terms of nuclear vibratory degrees of freedom. Walecka has done this for oscillations of a sharp-edged liquid drop model[6]:

$$M_{LM}=\frac{3Z}{4\pi c^3}\int_0^{4\pi} d\Omega Y_{LM}\int_0^{R(\Omega)} x^2 j_L(qx)dx, \tag{1}$$

where q is the momentum transfer,

$$R(\Omega)=c\left[1+\sum_{L'M'}\left(\frac{\hbar}{2\sqrt{EC}}\right)^{1/2}\times[b_{L'M'}+(-1)^{M'}b^{\dagger}_{L'-M'}]Y_{L'M'}\right],$$

Z is the atomic number, c is the nuclear radius, $b^{\dagger}_{LM}$ and b_{LM} are phonon creation and annihilation operators, and $(\hbar/2\sqrt{BC})$ is a collective model parameter. B and C are the usual collective model inertial and potential energy parameters. For the present work, $(\hbar/2\sqrt{BC})$ is determined by the $E2$ transition strength $(0^+\rightarrow 2_1^+)$. In the presence of quadrupole degrees of freedom only, the rms deformation of the nuclear ground state $\beta_0{}^2=5(\hbar/2\sqrt{BC})$. The collective model vibrational state wave functions can be written in terms of the phonon creation operators:

ground state,

$$|0\rangle;$$

first excited 2^+ or one-phonon state,

$$|1\rangle=b^{\dagger}_{2m}|0\rangle; \tag{2}$$

second excited 2^+ or two-phonon states,

$$|2\rangle=\left(\frac{2j+1}{2}\right)^{1/2}\sum_{m_1m_2}\begin{pmatrix}2 & 2 & j\\ -m_1 & m_2 & m\end{pmatrix}b^{\dagger}_{2m_1}b^{\dagger}_{2m_2}|0\rangle.$$

The electron scattering cross section can be computed using Eqs. (1) and (2).

$$\frac{d\sigma}{d\Omega}=4\pi\left(\frac{d\sigma}{d\Omega}\right)_{\text{Mott}}|\langle f||M_L||i\rangle|^2, \tag{3}$$

where the quantity inclosed by heavy vertical bars is the form factor and $(d\sigma/d\Omega)_{\text{Mott}}$ is the electron-nucleus scattering cross section for a point nucleus with unit charge. In order to compute the form factor for excitation of any given phonon state, one must expand the x integral in Eq. (1) about the integration limit $R(\Omega)=c$ in terms of β_0; $|\beta_0|\ll 1$. One then finds that

$$M_{LM}=\frac{3Z}{4\pi}\left[\left(\int_0^1 x^2 j_L(qcx)dx\right)\left(\int_0^{4\pi} d\Omega Y_{LM}\right)+\left(\frac{\beta_0}{\sqrt{5}}\right)[j_L(qc)]\sum_{M'}\left(\int_0^{4\pi} d\Omega Y_{LM}Y_{2M'}\right)\tilde{b}_{2M'}+\left(\frac{\beta_0}{\sqrt{5}}\right)^2\left(\frac{L+2}{2}j_L(qc)-\frac{qc}{2}j_{L+1}(qc)\right)\sum_{M'M''}\left(\int_0^{4\pi} d\Omega Y_{LM}Y_{2M'}Y_{2M''}\right)\tilde{b}_{2M'}\tilde{b}_{2M''}\right]+\dots, \tag{4}$$

where $\tilde{b}_{LM}=b_{LM}+(-1)^M b^{\dagger}_{L-M}$. The leading term in Eq. (4) dominates the elastic scattering process, while the successively higher order terms are responsible for transitions between an initial state and final states of successively higher (or lower) phonon number. Since experimentally we find β_0 to be of order 0.2, the higher order transition strengths diminish rapidly with increasing phonon number. Taking matrix elements of Eq. (4) between the ground state wave functions and normalized mixed phonon number wave functions,

$$|2_1^+\rangle=(1-a^2)^{1/2}|1\rangle-a|2\rangle$$

and (5)

$$|2_2^+\rangle=a|1\rangle+(1-a^2)^{1/2}|2\rangle,$$

leads to the Born approximation results for the cross sections presented in Refs. 2 and 3. In the present analysis we improve upon those results by using distorted-wave Born-approximation (DWBA) calculations to fit our data. For this purpose we require the radial form of the nuclear transition charge density ρ^{tr}. The origin of ρ^{tr} is best shown in Eq. (1), which can be rewritten as

$$M_{LM}=\int_0^{\infty} x^2 j_L(qx)dx\left[\int_0^{4\pi} d\Omega Y_{LM}\rho(r,\Omega)\right] \tag{6}$$

The quantity in square brackets is the transition charge, ρ^{tr}_{LM}. The reduced matrix element of ρ^{tr}_{LM} is required as input to DWBA codes. For simplicity we have chosen the form of $\rho(r,\Omega)$ as the two-parameter Fermi model

$$\rho(r,\Omega)=\rho_0\{1+\exp[r-R(\Omega)]/z\}^{-1}, \tag{7}$$

with

$$\rho_0=\frac{3Z}{4\pi c^3}(1+\pi^2 z^2/c^2)^{-1},$$

$R(\Omega)$ given in Eq. (1), c now becomes the half-density radius, and z a surface thickness parameter. The reduced transition probability in this formalism is given by

$$B(EL)\uparrow=\left|\int_0^{\infty} r^{L+2}\langle f\,\|\rho^{tr}_L\|\,i\rangle dr\right|^2. \tag{8}$$

Following exactly the same lines of reasoning which led to Eq. (4), expansion of Eq. (7) about $R(\Omega)=c$ leads to the transition charges for excitation of the pure one- and two-phonon states from the ground state:

$$\rho_1^{tr}(r)=\left(\frac{\beta_0}{\sqrt{5}}\right)\left(\frac{3Z}{4\pi c^3}\right)\left(\frac{c}{4Z}\right)(1+\pi^2 z^2/c^2)^{-1} \times\cosh^{-2}[(x-c)/2z]$$

and (9)

$$\rho_2^{tr}(r)=-\rho_1^{tr}(r)\left(\frac{\beta_0}{\sqrt{5}}\right)\left(\frac{c}{4z}\right)\left(\frac{10}{(35\pi)^{1/2}}\right) \times\tanh[(x-c)/2z].$$

Mixed phonon number transition charges must be constructed from $\rho_1^{tr}(r)$ and $\rho_2^{tr}(r)$ using normalized mixing amplitudes as in Eq. (5). The form of $\rho^{tr}(r)$ is shown in Fig. 2. Basically, since the transition operator results from a Taylor series expansion of the ground state charge distribution $\rho(r,\Omega)$, the n-phonon transition charge has the form

$$\rho_{n\ \text{phonon}}\sim\frac{(\beta_0)^n}{n!}\frac{\partial^n}{\partial R^n}\rho(r,R(\Omega)). \tag{10}$$

We should point out that there are alternative paths one can take in deriving the form of the transition charge, such as letting

$$\rho(r)\rightarrow\rho\left\{r\left[1+\sum_{LM}\left(\frac{\beta_0}{\sqrt{5}}\right)\bar{b}_{LM}Y_{LM}\right]\right\}; \tag{11}$$

however, they do not substantially alter the results presented here. It is possible that measurements of the form factor over a wider range of q would be sensitive to these different approaches.

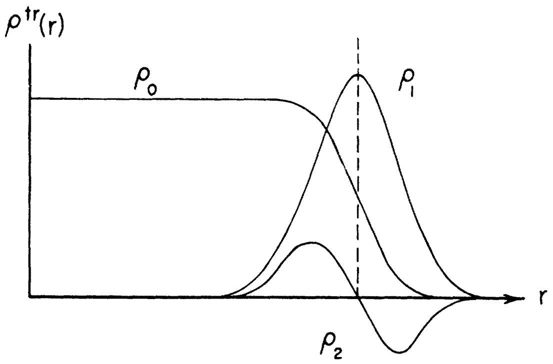

FIG. 2. Transition charges for pure one- and two-phonon excitations (ρ_1 and ρ_2). The ground state charge distribution ρ_0 is also shown. These curves are qualitative only.

III. EXPERIMENTAL EQUIPMENT AND TECHNIQUE

A. General

The experiment was performed at the National Bureau of Standards electron linear accelerator. Data were taken with incident beam energies ranging from 40 to 110 MeV at a nominal scattering angle of 127.5°. Typical overall experimental resolution was $\Delta p/p=0.1\%$, with beam currents up to several microamperes. The experiment was done in transmission geometry using thin foil targets of isotopically enriched material. (See Table I.) Beam currents were monitored with a Faraday cup. A secondary current monitor, consisting of a torroidal ferrite pulse transformer through which the beam passed, was placed upstream of the target. This monitor was calibrated relative to the Faraday cup and was used to monitor beam lost from the Faraday cup because of multiple scattering in the target. Scattered electrons were

TABLE I. Target Material.

^{12}C	23.2 mg/cm^2	Natural abundance
^{52}Cr	24.89 mg/cm^2	Natural abundance
^{110}Pd	18.84 mg/cm^2	97% ^{110}Pd
^{144}Cd	18.25 mg/cm^2	99.2% ^{114}Cd
^{116}Sn	9.25 mg/cm^2	95.7% ^{116}Sn

analyzed in a 169.8°, double focusing magnetic spectrometer, and detected in a 48 detector hodoscope of Si(Li) solid state detectors. The spectrometer azimuthal acceptance angle was 29.5 mrad and the polar acceptance angle was 128.0 mrad yielding a solid angle of 3.78 msr.

B. Detector system

The solid state detectors were fabricated 13 to a single silicon slab, each detector subtending $\Delta p/p = 0.027\%$, with a thickness of 1.5 mm in the scattered electron direction. Four such slabs were assembled side by side producing a 52 detector array in the focal plane, of which two on either end of the array were used only as guards. The entire array is operated at LN_2 temperature, and is movable along the focal plane in order to intercompare and average over results from several detectors. The semiconductor detectors (SC_j) are operated in coincidence with an array of plastic scintillators in order to suppress background and noise. The detector geometry is shown in Fig. 3. Scintillators $S1$ and $S4$ detect (i) electrons scattered from the target, (ii) electrons which arrive at the focal plane by compound processes, such as instrumental scattering of type (i) electrons from the spectrometer vacuum chamber, and (iii) room background events. The function of scintillators $S2$ and $S3$ is to detect (i) electrons which arrive at the focal plane by compound processes alone, and (ii) room background events. Scintillator $S1$ has twice the transverse extent of $S2$ or $S3$ (with the same thickness in the electron direction) and therefore by taking the difference between events of the form $SC_j \times S1 \times S4$ and events of the form $SC_j \times (S2+S3) \times S4$, we obtain the simple scattering events of interest. (The notation $A \times B$ refers to an electronic coincidence between events A and B.)

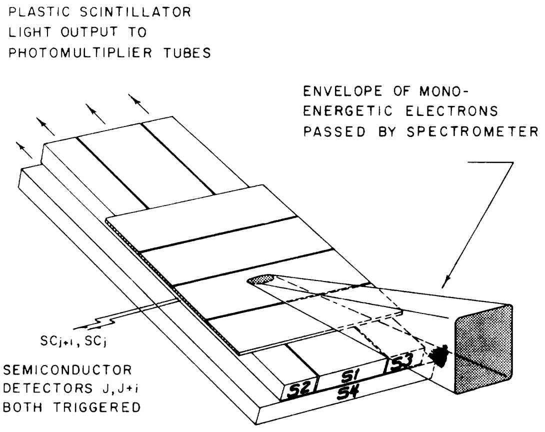

FIG. 3. Detector hodoscope geometry. $S1$, 2, 3, and 4 are plastic scintillators. The semiconductor detectors are Si(Li) type, operated at LN_2 temperature, and have a surface barrier on the side through which scattered electrons enter. This latter feature is to permit α-particle detection. The semiconductors are operated in the spectrometer vacuum and are separated from the scintillators by a thin Al window.

Signals from each of the semiconductors are processed separately by individual electronics chains consisting of charge sensitive preamplifiers, amplifiers, clipping lines, and discriminator/triggers. However, because the focal plane makes a 30° angle with the arrival direction of scattered electrons, two adjacent detectors are sometimes triggered by passage of a single electron. In order to prevent double counting we have constructed a signal processor[7] which performs a veto function between all pairs of adjacent detectors; $(j-1 \times j, j \times j+1)$, etc. If detectors j and $j+1$ are triggered, only the event from detector j is recorded. A more detailed description of the detector system including associated electronics, operating characteristics, instrumental effects, deadtime effects, etc., will be presented in a separate publication. Here we indicate only that the output of the detector system following each beam pulse is a 3 × 48 bit array corresponding to whether or not an event occurred in the "trues + background" channels ($SC_j \times S1 \times S4 \equiv C_j$), "background" channels [$SC_j \times (S2+S3) \times S4 \equiv B_j$], and/or in the "singles" channels (SC_j), these latter being useful for deadtime and accidental counting corrections. Multiple events per machine pulse per channel are detected only in separate summing channels for the entire ladder [i.e., $(\sum SCj) \times S1 \times S4$, $(\sum SCj) \times (S2+S3) \times S4$, and $(\sum SCj)$]. However, multiple event corrections to the separate channels, limited electronically to one event per machine pulse, can be made in a very straightforward fashion once we have the summing channel information.[8]

C. Experimental procedures

Data were taken for each of the vibrator nuclei targets together with a carbon target of natural isotopic abundance. The elastic scattering cross section measurements we present were made relative to the known carbon elastic scattering cross section based on Stanford results.[9] This procedure obviates the necessity of careful absolute spectrometer solid angle or detection efficiency measurements:

$$\left(\frac{d\sigma}{d\Omega}\right)_{\mathrm{el}}^{x} = \frac{(\mathrm{Area})_{\mathrm{el}}^{x}}{(\mathrm{Area})_{\mathrm{el}}^{^{12}\mathrm{C}}} \frac{t(^{12}\mathrm{C})}{t_x} \frac{A_x}{A(^{12}\mathrm{C})} \frac{d\sigma}{d\Omega}(^{12}\mathrm{C}), \qquad (12)$$

where $d\sigma/d\Omega(^{12}\mathrm{C})$ was calculated using the phase shift code HEINEL[10] with Stanford parameters for the ground state charge distribution. The scattering peak areas $(\mathrm{Area})^{x,\,^{12}\mathrm{C}}$ were obtained from line-shape fitting the bin-sorted doubly-differential cross section spectrum. (See next section.) The areas were corrected for radiative and ionization losses ("radiative corrections") as well as for variations in the Faraday cup efficiency due to multiple scattering of the beam in the target. The target thickness $t(\mathrm{g/cm}^2)$ is a nominal thickness based on measurement of the target area and total mass, and A is the target nucleus atomic weight.

The inelastic cross sections for each target were measured relative to the elastic scattering cross sections for that same target, and then normalized to the fitted elastic cross section. (See next section.) In this way any target nonuniformity or absolute target thickness uncertainty tends to cancel in the analysis:

$$\left(\frac{d\sigma}{d\Omega}\right)^x_{\mathrm{inel}} = f\frac{(\mathrm{Area})^x_{\mathrm{inel}}}{(\mathrm{Area})^x_{\mathrm{el}}}\left(\frac{d\sigma}{d\Omega}\right)^x_{\mathrm{el}}. \qquad (13)$$

The factor f takes into account all effects due to isotopic abundance. It is given to high accuracy by the reciprocal of the isotopic abundance provided that the other isotopes have a low abundance and do not have a strong state at the same excitation energy as the state of interest. For the present experiment these conditions are fulfilled except in the case of the 3.16 MeV, 2^+ state in ^{52}Cr. In that case we find that the other isotopes of chromium each have a state close to 3.16 MeV excitation. If the strength in each of these other states were equal to the ^{52}Cr strength, then we would set $f = 1.0$. Recent measurements at Saclay[11] have disclosed that for ^{50}Cr and ^{54}Cr these states are 3 times stronger than in ^{52}Cr. For lack of a measurement on ^{53}Cr we postulate a state at 3.16 MeV with the same strength as in ^{52}Cr. Given the natural isotopic abundance of our target we arrive at an f of 0.882.

We chose to use the fitted elastic scattering cross section for normalization of the inelastic cross sections rather than the measured cross sections because of uncertainty in the target thickness. As will be discussed in the next section, the elastic cross sections were fitted by allowing the static charge distribution parameters to be determined by the elastic scattering data. We included an overall normalization of the elastic scattering data as an additional degree of freedom, corresponding to target thickness uncertainty, and to be determined by the data. Consistency of our results for the static charge distribution with other determinations then led us to accept the calculated elastic scattering cross sections as the appropriate ones to use for the inelastic normalizations.

The spectrometer magnetic field was measured with a rotating coil gaussmeter having a precision of one part in 10^4. Energy calibration of the spectrometer was established using the known excitation energy of the 15.1 MeV, 1^+ state in ^{12}C to calibrate gaussmeter readings. The spectrometer dispersion was deduced by observing shifts in the position of scattering peaks in the focal plane as the magnetic field was changed by small increments. First and second order dispersion characteristics as well as detector momentum acceptance were measured in this way. Relative detector efficiencies of the 48 semiconductor detectors were determined by measuring cross sections on a smooth portion of the elastic radiation tail. This was done for several magnetic field settings spaced by one-half of the momentum acceptance of the detector hodoscope ($\frac{1}{2}$ of 1.4%). In choosing this data format we are insensitive to uncertainty in the spectrometer dispersion or to any other effect which introduces a linear dependence of the count rate in any given detector, on the central momentum of that detector. A least-squares fit to the resulting energy spectrum was made assuming equal relative efficiencies. Then the reciprocal of the average ratio of (i) cross sections determined by each of the individual detectors at their separate energies, to (ii) the fitted cross sections at those same energies, was taken as the efficiency for each detector. These efficiencies were then used in a new determination of the energy spectrum, and the entire process iterated. It proved necessary to have cross section measurements for at least five distinct magnetic fields spaced by the nominal 0.7% momentum difference in order for this procedure to converge.

IV. DATA ANALYSIS

A. Bin sorting

The first stage of data reduction is to correct the counts from different detectors for dead-time and accidental counting effects (always less than a few percent), differences in detector momentum acceptance due to the second order spectrometer dispersion, and for differences in detector efficiencies. At this point we produce a spectrum, $d^2\sigma/d\Omega dE$ versus E. For simplicity of display and further analysis it is convenient to sort data from the different detectors into bins of equal energy intervals. Since the detectors have finite momentum acceptance the question naturally arises as to what should be done when a given detector overlays two or more energy bins. We have chosen not to split and sort the counts from a given detector into different bins because this introduces statistical correlations between adjacent channels and complicates the determination of standard deviations for scattering peak areas. Instead we have chosen an iterative procedure which minimizes such correlations. The process begins by dividing the entire region covered by the spectrum into 1 keV intervals, called microbins. Counts from any given detector $(C_j - B_j)$ were placed in that microbin overlapping the detector central energy. We placed $C_j + B_j$ into a second microbin array to be used later in computing standard deviations. We placed the product of beam charge (accumulated for the same period of time as that in which the counts were accumulated) and detector energy acceptance into a third microbin array $(Q_j \times \Delta E)$ which was used later in normalizing the sum of counts spectrum to produce the doubly-differential cross section $d^2\sigma/d\Omega dE$. The point of this first step is to produce a memory of all the original data with energy uncertainties small enough so as to be negligible compared to resolution. We then initiate an iterative macrobinning procedure which converts the microbin data (many channels containing zeros) into data with more meaningful statistics and bin widths, such as 10 or 20 keV. In this procedure the first step is to place the contents of each microbin into whatever macrobin overlaps the microbin center, with no regard as to how close the microbin center fell to the macrobin boundary. Stopping at this step can lead to distortion of high resolution data. We then enter a loop in which a parabolic fit is made to successive three-macrobin regions of the normalized cross section spectrum $(C_j - B_j)/(Q_j \times \Delta E_j)$; i.e., channels $j-1, j, j+1$, channels $j, j+1, j+2$, etc. The form of this parabolic fit is then used to convert the counts in any given microbin $(C_j - B_j)$ contained in the central macrobin (channel j in the group $j-1, j, j+1$), to results $(C_j' - B_j')$ which would have been obtained had that microbin had a central energy corresponding to the macrobin central energy. In this way we obtain a new macrobin structure to which we make new parabolic fits to successive three-channel regions. Returning always to the original microbin data we iterate the process of generating macrobin data from the parabolic fitting function correction factors applied to microbin data. Macrobins are, of course, generated for the other microbin data channels, $(C_j + B_j)$ and $(Q_j \times \Delta E_j)$. They are not, however, subjected to these same iterative conversion factors. The entire iterative binning procedure showed excellent convergence for the present data. Caution must be observed with data of poor statistical precision, where the parabolic fitting can lead to pathological conversion factors. Final results for the $d^2\sigma/d\Omega dE$ spectrum and associated standard deviation spectrum are obtained by making channel-by-channel normalization of the $(C_j' - B_j')$ and $(C_j + B_j)^{1/2}$ macrobin spectra by the $(Q_j \times \Delta E_j)$ spectrum, respectively.

B. Line-shape fitting

In order to extract the cross section for a scattering peak, we have made use of a phenomenological line-shape program developed earlier[12] to give us the area contained under a peak in the doubly-differential cross section spectrum $(d^2\sigma/d\Omega dE)$. This peak lies, in general, above a smooth background or continuum resulting from elastically scattered electrons which have suffered energy loss by radiation during the scattering process. For the small cross section of the 2_2^+ state transition it is essential to use such a line-shape program in order to extract reliable estimates of the peak area and standard deviation. Modifications to this program were made to include multiple level fitting and radiative corrections to the peak areas. We found it necessary to use the multiple line-fitting procedure because for several target nuclei and incident energies, levels were not completely resolved. In such cases one has the option of (i) searching for a single set of line shape parameters which described all the levels, (ii) fixing the spacing between levels and searching for independent line shape parameters for each level, or (iii) both (neither) of the above items (i) and (or) (ii). The standard deviations of the extracted peak areas are computed using the full variance-covariance matrix (error matrix). In the case that several levels are fitted with a common variable, such as the peak width, care must be exercised to use the proper elements of the full error matrix when computing the standard deviation of any given peak area. All the cross section or form factor results which we herein present have been obtained with the aid of the line-shape fitting program. All radiative corrections are performed within the fitting routine, and are described elsewhere.[13]

C. Elastic scattering analysis

Analysis of the elastic scattering data was performed with an iterative nonlinear least-squares fitting routine which extracts static nuclear charge distribution parameters (see Table II). The basic fitting function used in this routine is a phase shift calculation for the electron-nucleus scattering cross section. The HEINEL computer code was used to perform this calculation.[10] As mentioned earlier, our overall normalization degree of freedom as well as the charge distribution parameters were then determined by the data. The two-parameter Fermi model was used to describe the static nuclear charge distribution;

TABLE II. Elastic scattering cross sections in mb/sr. We use the notation 0.1394 − 02 = 0.1394 × 10^{-02}. The standard deviations associated with each measurement were in all cases smaller than 1%. For purposes of extracting ground state charge distribution parameters we assigned a 2% standard deviation based on estimated instrumental uncertainties.

E_i (MeV)	θ (deg)	^{52}Cr	^{110}Pd	^{114}Cd	^{116}Sn
39.38	127.74	0.3715 + 00	0.0953 + 00	0.1043 + 01	0.1194 + 01
49.44	127.74	0.1528 + 00	0.2677 + 00	0.2809 + 00	0.3167 + 00
59.84	127.71	0.5604 − 01	0.5752 − 01	0.5837 − 01	0.6860 − 01
75.22	127.71	0.1104 − 01	0.8504 − 02	0.1001 − 01	0.1299 − 01
75.02	127.81				0.1270 − 01
92.73	127.74	0.9344 − 03	0.4624 − 02	0.4981 − 02	0.6277 − 02
110.20	127.69	0.1414 − 03	0.1395 − 02	0.1494 − 02	0.1752 − 02

TABLE III. Ratios of inelastic scattering cross sections to $Z^2\sigma_{\text{Mott}}$.

^{52}Cr

E_i (MeV)	θ (deg)	1.43 MeV, 2^+ state	3.16 MeV, 2^+ state
39.38	127.74	(0.90 ± 0.04)-03	(0.55 ± 0.55)-05
49.44	127.74	(0.159 ± 0.006)-02	(0.29 ± 0.07)-04
59.84	127.71	(0.26 ± 0.02)-02	(0.89 ± 0.30)-04
75.22	127.71	(0.265 ± 0.007)-02	(0.842 ± 0.012)-04
92.73	127.74	(0.222 ± 0.005)-02	(0.428 ± 0.052)-04
110.20	127.69	(0.97 ± 0.02)-03	(0.222 ± 0.044)-04

^{110}Pd

E_i (MeV)	θ (deg)	0.374 MeV, 2_1^+ state	0.81 MeV, 2_2^+ state
39.38	127.74	(0.35 ± 0.03)-02	(0.45 ± 0.14)-04
49.44	127.74	(0.40 ± 0.02)-02	(0.10 ± 0.01)-03
59.84	127.71	(0.40 ± 0.02)-02	(0.10 ± 0.01)-03
75.22	127.71	(0.233 ± 0.003)-02	(0.86 ± 0.07)-04
92.73	127.74	(0.40 ± 0.05)-03	(0.48 ± 0.06)-04
110.20	127.69	(0.23 ± 0.01)-03	(0.17 ± 0.17)-05

^{114}Cd

E_i (MeV)	θ (deg)	0.558 MeV, 2_1^+ state	1.208 MeV, 2_2^+ state
39.38	127.74	(0.20 ± 0.02)-02	(0.46 ± 0.07)-04
49.44	127.74	(0.28 ± 0.02)-02	(0.40 ± 0.06)-04
59.84	127.71	(0.220 ± 0.014)-02	(0.58 ± 0.11)-04
75.22	127.71	(0.118 ± 0.005)-02	(0.34 ± 0.04)-04
92.73	127.74	(0.204 ± 0.007)-03	(0.11 ± 0.04)-04
110.20	127.69	(0.155 ± 0.007)-03	(0.61 ± 0.35)-05

^{116}Sn

E_i (MeV)	θ (deg)	1.294 MeV, 2_1^+ state	2.112 MeV, 2_2^+ state	2.266 MeV, 3^- state
39.38	127.74	(0.65 ± 0.04)-03	(0.68 ± 1.05)-05	(0.18 ± 0.02)-03
49.44	127.74	(0.88 ± 0.04)-03	(0.26 ± 0.69)-05	(0.40 ± 0.01)-03
59.84	127.71	(0.84 ± 0.03)-03	(0.21 ± 0.06)-04	(0.63 ± 0.02)-03
75.22	127.71	(0.36 ± 0.02)-03	(0.5 ± 7.4)-06	(0.84 ± 0.02)-03
75.02	127.81	(0.34 ± 0.02)-03	(0.47 ± 0.39)-05	(0.82 ± 0.01)-03
92.73	127.74	(0.50 ± 0.09)-04	(0 ± 0.19)-04	(0.60 ± 0.01)-03
110.20	127.69	(0.85 ± 0.10)-04	(0 ± 0.8)-05	(0.14 ± 0.01)-03

$$\rho(r) = \rho_0\{1 + \exp[(r-c)/z]\}^{-1},$$

$$t = 4z\ \ln 3, \tag{14}$$

and

$$\langle r^2\rangle = (3/5)c^2 + (7\pi^2/5)z^2,$$

where c is the half-density radius, t is the skin thickness (the change in radius for which the density falls from 90 to 10% of the central density), $\langle r^2\rangle^{1/2}$ is the rms nuclear charge radius, and ρ_0 is a constant given in Eq. (7). For the momentum transfer range covered in this experiment we expect that the simple two-parameter Fermi model is adequate to describe our results. We find, however, that our data lie in a q region which is sensitive to details of $\rho(r)$ such as c and z, and which does not depend strongly on $\langle r^2\rangle^{1/2}$ alone. We therefore sought a means of combining our data with muonic x-ray results for the rms radius. Using the technique of Lagrange multipliers, we were able to perform a fit to our data, determining c and z subject to constraint of the rms radius. A discussion of this method and development of the error matrix under conditions of constraints will be presented in a separate publication. The point of this effort is that we are able to compare fits to our data with and without constraint of the rms radius in order to check (i) if the fits were strongly influenced by this external constraint, and (ii) if perhaps imposition of this constraint caused substantial change in the normalization degree of freedom.

D. Inelastic data analysis

Analysis of the inelastic data (Table III) was performed using another phase shift code HEINEL INELASTIC.[10] We sought to extract reduced nuclear transition probabilities [$B(EL)$'s] and parametrization of the nuclear transition charge density, $\rho^{tr}(r)$, as described in Sec. II. The computer calculation for inelastic scattering takes considerably longer than for the elastic scattering case, and is most efficient if the data are in the form of an angular distribution. Our data are in the form of an energy distribution at fixed angle, so we proceeded to convert the data to an angular distribution. This technique is iterative and requires initial estimates of the nuclear transition charge density as input. The incident energy for this equivalent angular distribution was chosen as the highest energy used in the actual experiment. We begin a loop at this point, using the phase shift code to compute cross sections ($d\sigma/d\Omega$ actual) for the kinematic circumstances of the actual experimental data points. One then examines the angular distribution for the highest energy calculation, and extracts cross sections ($d\sigma/d\Omega$ equivalent) at those angles for which the corresponding effective momentum transfers[14] are the same as the effective momentum transfers of the actual data points. The ratio of ($d\sigma/d\Omega$ equivalent) to ($d\sigma/d\Omega$ actual) converts the actual experimental cross sections and standard deviations to equivalent experimental cross sections and equivalent standard deviations. At this point model fits are made to the angular distribution to extract a new form of the transition charge. We then close the loop and return to the conversion factor calculation. We found that the process of making the conversion and transition charge determination is rapidly convergent requiring at most three iterations to arrive at a condition where further iterations produce at most

TABLE IV. Ground state charge distribution parameters.

	^{52}Cr	^{110}Pd	^{114}Cd	^{116}Sn
		Free fitting		
c (fm)	3.988 ± 0.010	5.301 ± 0.023	5.314 ± 0.023	5.358 ± 0.022
z (fm)	0.5348 ± 0.0094	0.5808 ± 0.0085	0.5715 ± 0.0087	0.5497 ± 0.0091
$\langle r^2\rangle^{1/2}$ (fm)	3.674 ± 0.015	4.639 ± 0.019	4.632 ± 0.017	4.626 ± 0.015
Norm	1.064 ± 0.020	1.181 ± 0.024	1.110 ± 0.023	1.158 ± 0.021
$\chi^2/(N-P)$	0.6	2.2	1.4	1.0
$N-P$	3	3	3	4
		Constrained fitting		
c (fm)	3.994 ± 0.087	5.266 ± 0.018	5.308 ± 0.018	5.374 ± 0.019
z (fm)	0.5226 ± 0.0029	0.5703 ± 0.0072	0.5698 ± 0.0075	0.5559 ± 0.0079
$\langle r^2\rangle^{1/2}$ (fm)	3.653 ± 0.046[a]	4.595 ± 0.003[b]	4.624 ± 0.008[c]	4.642 ± 0.006[d]
Norm	1.040 ± 0.008	1.128 ± 0.010	1.102 ± 0.008	1.184 ± 0.011
$\chi^2/(N-P)$	1.0	3.2	1.0	1.3
$N-P$	4	4	4	5

[a] See Ref. 22.
[b] See Ref. 23.
[c] See Ref. 24.
[d] See Ref. 25.

0.1% effects on the converted data. The rapidity of convergence is, however, dependent on making a reasonable first estimate of the nuclear transition charge density.

V. RESULTS

A. Elastic scattering

Analysis of the elastic scattering data provides two sets of charge distribution parameters, with and without constraint of the rms radius. These parameters are presented in Table IV. Statistical precision of the elastic scattering data was generrally greater than one percent. However, because of various instrumental uncertainties, we estimated that the standard deviation for each data point should be about 2%. In deriving the static charge distribution parameters we used this constant 2% standard deviation.

The ^{110}Pd results are the only ones which show a significant increase in χ^2 coming from imposition of the rms radius constraint. The value of the rms radius that we used was derived from two different experiments. The first[15] was a study of the atomic $2p \rightarrow 1s$ μ transition in naturally occurring palladium which yielded an isotopic mean μ–x-ray energy and isotopic mean rms radius. In order to obtain a value for the ^{110}Pd rms radius we made use of optical isotope shift data for differences in the rms radii of the different Pd isotopes.[16] With the assumption that the unmeasured ^{105}Pd optical isotope shift is given by averaging the ^{104}Pd and ^{106}Pd results, we found that

$$\langle r^2\rangle^{1/2}(^{110}\mathrm{Pd}) = 4.595 \pm 0.033 \text{ fm}.$$

This value is in fair statistical agreement with our unconstrainted fit result; however, our choice of exactly 4.595 fm for the rms radius constraint was unjustified. In a more complete treatment of this problem one should replace the rigid constraint by a distribution function. Details of this point will be discussed in the future publication relating to constrained least-squares fitting. The failure to achieve a good χ^2 for the unconstrained fitting of the ^{110}Pd data is not understood; however, it is possible that the two-parameter Fermi model is simply inadequate to describe the data.

In the case of the other targets (^{52}Cr, ^{114}Cd, and ^{116}Sn) fits to the cross sections have acceptable χ^2's. The unconstrained and constrained fitting produces statistically equivalent parameters for the static charge distributions. The unconstrained fitted values for the rms radii are in statistical agreement with other measurements of the rms radii. We have chosen to compare and constrain our data with the latest muonic x-ray results for the rms radii wherever possible. (See the references cited in Table IV.) This was not possible for ^{52}Cr, so we used the weighted average of the early (e, e') results of Bellicard *et al.* and muonic x-ray results of Johnson *et al.* cited in Ref. 17. These experiments used targets of natural isotopic abundance. Having established the consistency of the present elastic scattering cross sections and charge distribution parameters with the previously determined ground state charge distribution parameters, we used calculated cross sections based on unconstrained fitting determinations of the ground state charge distribution to normalize our inelastic scattering results.

B. Inelastic scattering

We have used the anharmonic vibrator model transition charge distribution to fit the 2_1^+ and 2_2^+ vibrational state cross sections in ^{110}Pd, ^{114}Cd, and ^{116}Sn. This model does not accurately describe the data for ^{52}Cr (the 1.43 and 3.16 MeV, 2^+ states); however, the failure should not come as a total surprise because the ^{52}Cr level scheme is not as vibratorlike as the other nuclei studied here. The model used most successfully in describing the level scheme and transition character of ^{52}Cr is the $(f_{7/2})^4$ seniority coupling shell model.[18] We have not explored this avenue for interpreting our data; however, it has recently been used in the work of de Bie.[19] Our main interest was in seeing if the higher excitation energy 2^+ states had a different q dependence than the lowest energy 2^+ state. This difference is an interesting

TABLE V. ^{52}Cr Tassie model transition charge distribution parameters.

	Excited state	c_{tr}/c	z_{tr}/z	$B(E2)$ e^2fm^4	$\chi^2/(N-P)$	$N-P$
1.43 MeV	Present data	0.956± 0.040	0.905± 0.115	634± 39	2.2	3
2^+ State	de Bie (Ref. 19)	0.933± 0.010	0.991	761± 30	1.6	8
	Towsley *et al*. (Ref. 20)			666± 29		
3.16 MeV	Present data	0.901± 0.041	0.991[a]	12.4± 2.3	2.5	4
2^+ State	de Bie	0.931± 0.040	0.991[a]	15.5± 2.0	1.0	5

[a] By assumption, from de Bie.

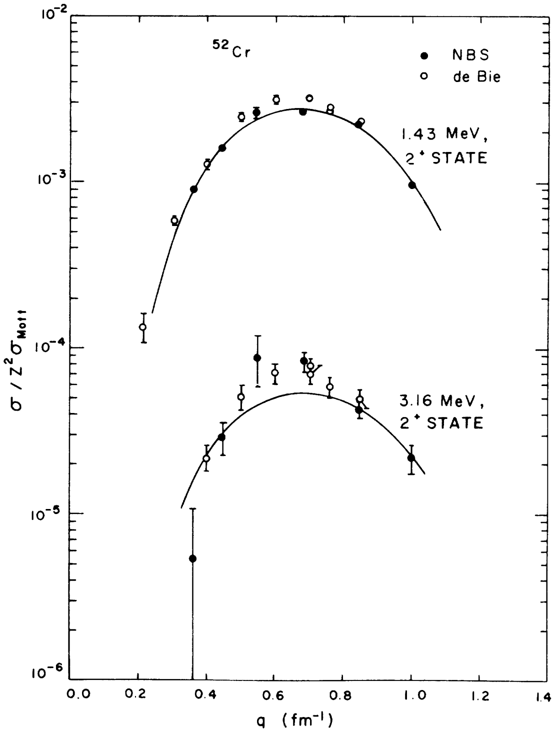

FIG. 4. Cross section for ^{52}Cr in units of $Z^2\ \sigma_{\text{Mott}}$ for the 1.43 and 3.16 MeV, σ_{Mott} 2^+ states. Also shown are the data of de Bie. Tassie model fits to the NBS data alone are given by the solid curves.

consequence of mixing the pure one- and two-phonon transitions matrix elements, and the effect is to shift the maximum of the physical 2_2^+ state form factor to higher or lower momentum transfer with respect to the 2_1^+ state form factor, depending on the phase and magnitude of the admixture. The ^{52}Cr 1.43 and 3.16 MeV state form factors show no evidence for this shifting. We therefore adopted the Tassie model transition charge for both states, seeking only to extract effective transition radius and skin thickness parameters, and reduced transition probabilities $B(E2)\uparrow$. In the Tassie model

$$\rho^{\text{tr}}(r) \propto r \frac{\partial}{\partial r} \rho(r), \tag{15}$$

where $\rho(r)$ is the ground state charge distribution (two-parameter Fermi model) with an effective transition radius (c_{tr}) and skin thickness parameter (z_{tr}). The results of our fitting the ^{52}Cr data are given in Table V and Fig. 4. In this case, as for the ^{110}Pd, ^{114}Cd, and ^{116}Sn inelastic fitting, we used standard deviations for the inelastic cross sections derived from use of the full variance-covariance matrix obtained in the line-shape fitting procedure. The χ^2 values for the ^{52}Cr cross section fits are rather large; however, not significantly larger than the values obtained by de Bie for these same states. Furthermore our c_{tr} and z_{tr} values are equivalent, within the uncertainties, to the de Bie values. The only disagreement between the present results and the de Bie data is the $B(E2)\uparrow$ value for the 1.43 MeV, 2^+ state. Our value is below de Bie's by four standard deviations or roughly 15%. One possible source of this discrepancy lies in our use of a natural rather than isotopically enriched chromium target. It is possible that the states in the other isotopes of chromium near 1.43 MeV excitation energy could be biasing our radiation tail or background determinations for the 1.43 MeV state cross sections to higher values, thereby reducing somewhat our determination of the 1.43 MeV form factor and $B(E2)\uparrow$ value. However, our $B(E2)$ is in excellent agreement with the recent Coulomb excitation value of Towsley *et al.*,[20] and with their results for a best value of $B(E2)$ obtained by taking the weighted mean of their own and previous measurements. Our fit to the 3.16 MeV, 2^+ state gives a $B(E2)$ value of $12.4 \pm 2.3\ e^2\text{fm}^4$ which is consistent with de Bie's value of $15.5 \pm 2.0\ e^2\text{fm}^4$. We were unable, however, to make a simultaneous least-squares determination of c_{tr}, z_{tr}, and $B(E2)\uparrow$. Since our 3.16

TABLE VI. Anharmonic vibrator model parameters.

	^{110}Pd	^{114}Cd	^{116}Sn
c_{tr} (fm)	5.169 ± 0.022	5.214 ± 0.021	5.446 ± 0.048
z_{tr} (fm)	0.529 ± 0.039	0.593 ± 0.040	0.550 ± 0.047
β_0	0.277 ± 0.012	0.218 ± 0.009	0.124 ± 0.004
a	0.2011 ± 0.0044	0.1749 ± 0.0060	0.14 ± 0.02 [a]
$B(E2_1^+)$ ($e^2\text{fm}^4$)	7966 ± 682	5753 ± 475	2288 ± 148
$\chi^2(2_1^+)/(N-P)$	1.3	1.5	1.2
$N-P$	3	3	4
$B(E2_2^+)$ ($e^2\text{fm}^4$)	72.9 ± 8.0	50.2 ± 7.6	19.8^{+10}_{-7}
$\chi^2(2_2^+)/(N-P)$	3.0	3.0	1.0
$N-P$	5	5	6

[a] Fit estimated by eye.

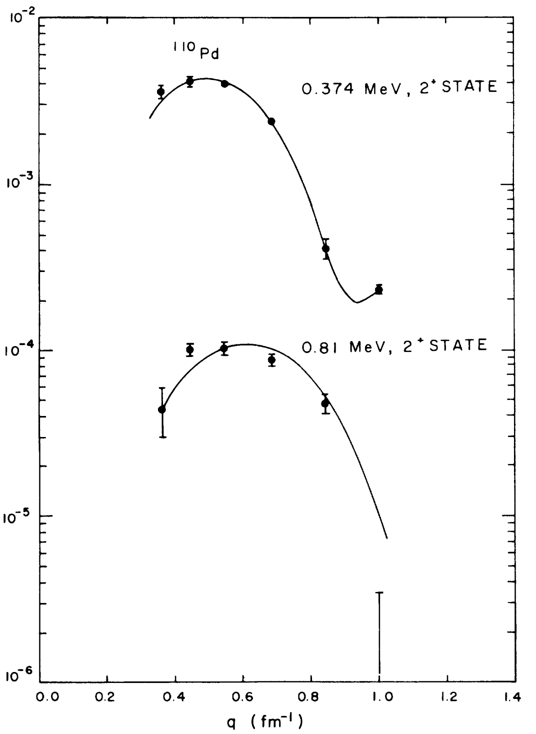

FIG. 5. Cross sections for ^{110}Fd in units of $Z^2\sigma_{\rm Mott}$ for the 0.374 and 0.81 MeV, $\sigma_{\rm Mott}$ 2^+ states. The solid curves are fits based on the anharmonic vibrator model.

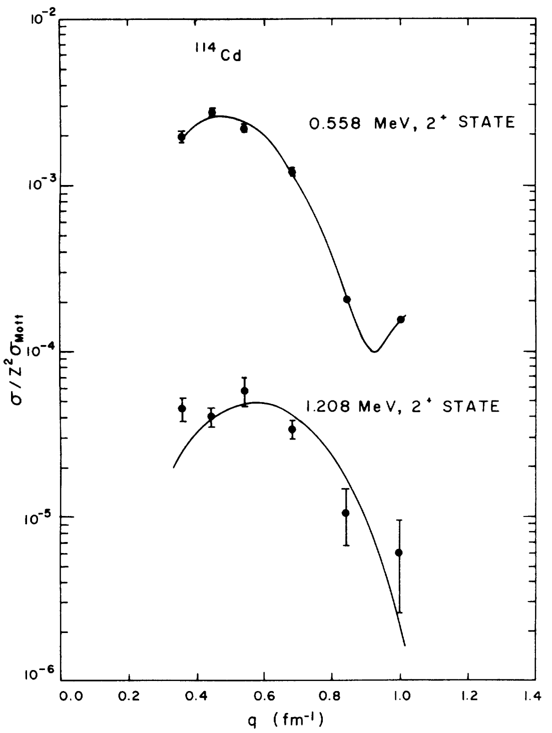

FIG. 6. Cross sections for ^{114}Cd in units of $Z^2\sigma_{\rm Mott}$ for the 0.558 and 1.208 MeV, $\sigma_{\rm Mott}$ 2^+ states. The solid curves are fits based on the anharmonic vibrator model.

MeV state data are in agreement with the data of de Bie, we took $z_{\rm tr}$ from de Bie and were then able to make a least-squares determination of $c_{\rm tr}$ and $B(E2)$.

Turning next to the vibrator nuclei, we present results of our determination of the anharmonic vibrator model, transition charge distribution parameters in Table VI. In obtaining these results we first made a least-squares fit to the 2_1^+ state cross section in the vibrator model parameter space using estimated values of the mixing amplitude "a" [see Eq. (5)], given in our preliminary analysis of these data.[3] From these fits we extracted $c_{\rm tr}$, $z_{\rm tr}$, and β_0. Then using these same 2_1^+ parameters, we made a least-squares determination of the mixing amplitude by fitting the 2_2^+ state cross section with the mixing amplitude as the only degree of freedom. Results of these fits are shown in Figs. 5–7 for ^{110}Pd, and ^{116}Sn, respectively. χ^2's for the various 2_1^+-state fits are reasonably good [$\chi^2/(N-P)$ of 1.2 to 1.5]; however, for the 2_2^+

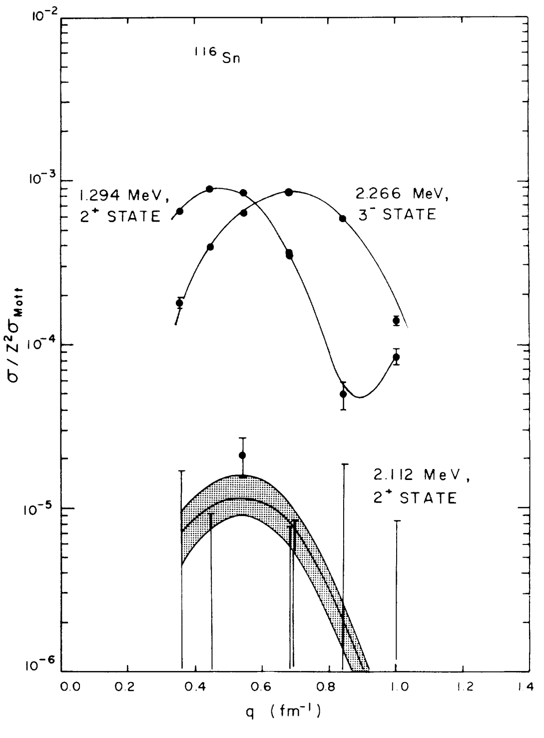

FIG. 7. Cross sections for ^{116}Sn in units of $Z^2\sigma_{\rm Mott}$ for the 1.294 and 2.112 MeV, $\sigma_{\rm Mott}$ 2^+ states, and for the 2.266 MeV, 3^- state. The curves fitted to the 2^+ state data are based on the anharmonic vibrator model, while the 3^- state fit is based on the Tassie model. The shaded region about the 2.112 MeV state data indicates $a \pm 1$ standard deviation band around the estimated best fit curve. The upper and lower limits to the band correspond to admixture parameters of 0.16 and 0.12, respectively.

TABLE VII. ^{116}Sn, 2.266 MeV, 3^- state Tassie model parameters.

	$c_{\rm tr}$ (fm)	$z_{\rm tr}$ (fm)	$B(E3)\uparrow$ (e^2fm^6)	$\chi^2/N-P$	$N-P$
This experiment	4.367 (192)	0.670 (42)	$(1.63\pm0.13)\times10^5$	4.5 [a]	4
Curtis *et al.* (Ref. 21)	3.696	0.522	7.4×10^4	2.1	5

[a] By not including the highest energy data point, this value drops to 2.4.

state fits we see some evidence for model inadequacy $[\chi^2(N-P)\approx3]$. The lack of good statistical precision for the data makes it difficult to determine Tassie model parameters independently for the 2_2^+ states, so we made no other model fits to these data. One can see from Tables IV and VII that best fit values for $c_{\rm tr}$ and $z_{\rm tr}$ are slightly different from best fit values for the static charge distribution parameters c and z. In principle the two parameter sets should be identical. The observed differences may be attributed to oversimplifications in the present vibrator model such as the somewhat arbitrary choice of the functional form of $\rho_{\rm tr}(r)$ (see Sec. II) and the neglect of other many-phonon amplitudes in the ground and excited state wave functions. By relaxing the requirement that $c_{\rm tr}\equiv c$ and $z_{\rm tr}\equiv z$ we attempt to allow for effects induced by our model deficiency, and still access the dominant anharmonicities.

In the ^{116}Sn spectrum there is a strong 3^- state near the 2_2^+ state which makes measurement of the 2_2^+ state form factor extremely difficult without better experimental resolution. We made use of the multiple-line fitting routine, discussed earlier, in extracting the 2_2^+ state cross sections presented here. With the exception of one data point these latter measurements are useful only for setting upper limits on the cross sections. As a by-product we obtained the 3^- state cross sections, from which we derived the transition parameters given in Table VII. These are to be compared with the results of Curtis *et al.*[21] also shown in Table VII. The different results disagree substantially. The source of the discrepancy is not clear. However, since the present data cover most of the first diffraction peak of the form factor and the data of Curtis *et al.* only cover the low q region ($q<0.6$ fm^{-1}), our results are probably better suited to determining the transition charge details.

Based on the anharmonic vibrator model fits to the ^{110}Pd, ^{114}Cd, and ^{116}Sn data we have made estimates of the 2_1^+ state static quadrupole moment $Q(2_1^+)$ and branching ratios $B(E2;2_2^+\to0^+)/B(E2;2_2^+\to2_1^+)$ and $B(E2;2_2^+\to2_1^+)/B(E2;2_1^+\to0^+)$. These results are presented in Table VIII along with direct measurement. All of our estimates were computed using the formalism presented in Sec. II. We have compared these computations with those using the sharp-edged-nucleus formalism of Ref. 2 and found that there is little difference between the two sets of results provided that an effective radius ($c_{\rm eff}$) is used in the sharp-edged-nucleus calculation:

$$3/5c_{\rm eff}{}^2=3/5(c_{\rm tr})^2[1+7/3\pi^2(z_{\rm tr}/c_{\rm tr})^2], \qquad (16)$$

in analogy with the static charge distribution where one can describe an effective sharp-edged-nucleus which has the same rms radius as the two-param-

TABLE VIII. Excited state quadrupole moments and branching ratios.

	^{110}Pd	^{114}Cd	^{116}Sn
$Q(2_1^+)$ (b)	$-0.47\ \pm0.03$	$-0.34\ \pm0.03$	$-0.17\ \pm0.04$
	$-0.483\ \pm0.049$ [a]	$-0.32\ \pm0.08$ [b]	$+0.09\ \pm0.13$ [c]
	or $-0.266\ \pm0.049$ [a]		
	$-0.72\ \pm0.12$ [d]		
	or $-0.45\ \pm0.12$ [d]		
$B(E2;2_2^+\to0^+)/B(E2;2_2^+\to2_1^+)$	0.0058 ± 0.0013	0.0052 ± 0.0013	0.0047 ± 0.0012
	$0.014\ \pm0.001$ [e]		
$B(E2;2_2^+\to2_1^+)/B(E2;2_1^+\to0^+)$	1.58	1.69	1.82
	$0.99\ \pm0.19$ [e]		

[a] See Ref. 26.
[b] See Ref. 28.
[c] See Ref. 29.
[d] See Ref. 27.
[e] See Ref. 30.

eter Fermi model. As can be seen from Table VIII our values for the 2_1^+ state quadrupole moments agree quite well with previously measured values. Our branching ratio estimates do not agree as well with the measured ratios. It is difficult to say wherein lies the source of this latter model inadequacy. One can again speculate that the problem lies in neglecting many-phonon amplitudes in the ground state as well as other many-phonon amplitudes in the 2_1^+ and 2_2^+ states. As was pointed out in the Introduction, however, the idea behind this experiment was to test a very simple anharmonic vibrator model, and we feel that in so doing we have identified the major components of the collective model wave functions. It, of course, remains a problem to understand our results in terms of microscopic wave functions.

We wish to extend our thanks to Dr. Peter Trower for the loan of the tin target, and to the NBS Linac Operations group for providing good accelerator performance.

---

*Work supported in part by NSF Grant GP-34391.

†Present address: Operations Research, Inc., Silver Spring, Maryland 20910.

[1] D. Cline, Univ. of Rochester Report No. UR-NSRL-37, 1970 (unpublished).

[2] J. W. Lightbody, Jr., Phys. Lett. 38B, 475 (1972).

[3] S. Penner, J. W. Lightbody, Jr., S. P. Fivozinsky, H. Crannell, P. L. Hallowell, and M. Finn, in *Proceedings of the International Conference on Nuclear Structure Studies Using Electron Scattering and Photoreactions, Sendai, Japan, 1972,* edited by K. Shada, and H. Ui (Tohoko Univ. Sendai, Japan, 1972).

[4] G. Gneuss and W. Greiner, Nucl. Phys. A171, 449 (1971).

[5] A. Bohr and B. R. Mottelson, *Nuclear Structure* (Benjamin, New York, 1975), Vol. 2. See also L. Sips, Phys. Lett. 36B, 193 (1971).

[6] J. D. Walecka, Phys. Rev. 126, 653 (1962).

[7] J. K. Whittaker, IEEE Trans. Nucl. Sci. NS-19(3), 444 (1972).

[8] J. W. Lightbody, Jr., and S. Penner, IEEE Trans. Nucl. Sci. NS-15, 419 (1968).

[9] I. Sick and J. S. McCarthy, Nucl. Phys. A150, 631 (1970).

[10] J. Heisenberg, MIT (private communication).

[11] J. B. Bellicard (private communication).

[12] B. T. Chertok, C. Sheffield, J. W. Lightbody, Jr., S. Penner, and D. Blum, Phys. Rev. C 8, 23 (1973).

[13] J. C. Bergstrom, H. Crannell, F. J. Kline, J. T. O'Brien, J. W. Lightbody, Jr., and S. P. Fivozinsky, Phys. Rev. C 4, 1514 (1971).

[14] The effective momentum transfer $q_{\mathrm{eff}} \equiv q[1+(3Z\alpha/2kR)]$, where k is the wave number of the incident electron and R is the radius of the equivalent uniform charge distribution.

[15] G. Backenstoss, K. Goebel, B. Stadler, U. Hegel, and D. Quitmann, Nucl. Phys. 62, 449 (1965).

[16] P. Brix and H. Kopfermann, Rev. Mod. Phys. 30, 517 (1958); and H. Schaller, Ph.D. dissertation, T. H. Munich, 1966 (unpublished).

[17] H. R. Collard, L. R. B. Elton, and R. Hofstadter, in *Nuclear Radii,* Group I, Vol. 2 of the Landbolt-Bornstein New Series, edited by H. Schopper (Springer-Verlag, Berlin, 1967), pp. 12 and 35.

[18] J. D. McCullen, B. F. Bayman, and L. Zamick, Phys. Rev. 134, B515 (1964).

[19] J. E. P. de Bie, dissertation, Instituut voor Kernphysisch Onderzoek, Amsterdam, The Netherlands, 1974 (unpublished).

[20] C. W. Towsley D. Cline, and R. N. Horoshko, Nucl. Phys. A250, 381 (1975).

[21] T. H. Curtis, R. A. Eisenstein, D. W. Madsen, and C. K. Bockelman, Phys. Rev. 184, 1162 (1969).

[22] Weighted average of the (e,e') and μ–x-ray results cited in Ref. 17.

[23] μ–x-ray andatomic isomer shift data (Refs. 15 and 16) discussed in text.

[24] J. W. Kast, S. Bernow, S. C. Cheng, D. Hitlin, W. Y. Lee, E. R. Macagno, A. M. Rushton, and C. S. Wu, Nucl. Phys. A169, 62 (1971).

[25] See Ref. 23. This result is not in good accord with the tabulated (e,e') result of C. W. de Jager, H. de Vries, and C. de Vries, At. Data Nucl. Data Tables 14, 479 (1974).

[26] R. Beyer, R. P. Scharenberg, and J. Thomson, Phys. Rev. C 2, 1469 (1970). The two values correspond to the different possible phases of the interference moment.

[27] R. P. Harper, A. Christy, I. Hall, I. M. Nagib, and B. Wakefield, Nucl. Phys. A162, 161 (1971); see also Ref. 26.

[28] Z. Berant, R. A. Eisenstein, J. S. Greenberg, Y. Horowitz, U. Similansky, P. M. Tandon, A. M. Kleinfeld, and H. G. Maggi, Phys. Rev. Lett. 27, 110 (1971).

[29] A. M. Kleinfeld, R. Covello-Moro, H. Cgata, G. G. Seaman, S. G. Steadman, and J. de Boer, Nucl. Phys. A154, 499 (1970).

[30] R. L. Robinson, F. K. McGowan, P. H. Stelson, W. T. Milner, and R. O. Sayer, Nucl. Phys. A124, 553 (1969).

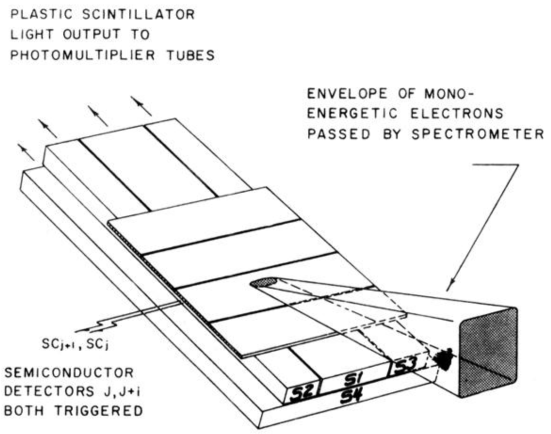

FIG. 3. Detector hodoscope geometry. *S*1, 2, 3, and 4 are plastic scintillators. The semiconductor detectors are Si(Li) type, operated at LN_2 temperature, and have a surface barrier on the side through which scattered electrons enter. This latter feature is to permit α-particle detection. The semiconductors are operated in the spectrometer vacuum and are separated from the scintillators by a thin A1 window.

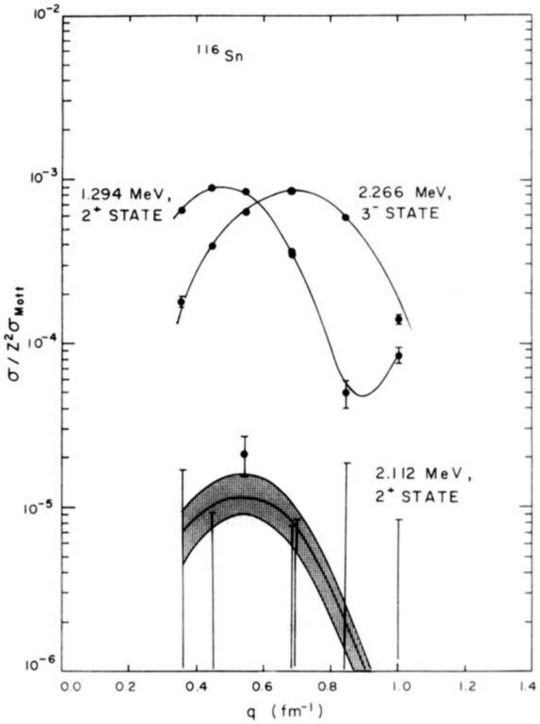

FIG. 7. Cross sections for ^{116}Sn in units of $Z^2\sigma_{\mathrm{Mott}}$ for the 1.294 and 2.112 MeV, σ_{Mott} 2^+ states, and for the 2.266 MeV, 3^- state. The curves fitted to the 2^+ state data are based on the anharmonic vibrator model, while the 3^- state fit is based on the Tassie model. The shaded region about the 2.112 MeV state data indicates *a* ± 1 standard deviation band around the estimated best fit curve. The upper and lower limits to the band correspond to admixture parameters of 0.16 and 0.12, respectively.